60th ARFTG Conf. Dig., Washington, D.C., Dec. 5-6, 2002, pp. 85-97. Presented by Kate Remley.

Nose-to-Nose Oscilloscope Calibration Phase Error Inherent in the Sampling Circuitry*

Kate A. Remley
RF Electronics Group 813.01
National Institute of Standards and Technology
325 Broadway; Boulder, CO 80305
Phone: +1-303-497-3652; Email: remley@boulder.nist.gov

Abstract: We use SPICE simulations to study the dependence of the phase error in the nose-to-nose oscilloscope calibration on the oscilloscope's sampling circuitry. We determine which components of the internal sampling circuitry of the oscilloscope contribute most significantly to errors in the nose-to-nose calibration. We then predict an expected range of phase errors from a range of realistic component values.

1. Introduction

We numerically quantify the inherent error in the nose-to-nose oscilloscope calibration due to internal sampling circuitry using a SPICE[1]-based methodology developed in [1-3]. We perform parametric variation of component values of a representative sampling-circuit model and determine the effect on the error in the nose-to-nose-derived impulse response of the sampler. The goals of the study include: (1) determining which components of the internal sampling circuitry of the oscilloscope contribute most significantly to errors in the estimated phase response provided by the nose-to-nose calibration; (2) predicting an expected range of phase errors from a realistic range of component values. This second point is important because the exact values of component and parameter in real oscilloscopes are unknown, due to measurement limitations, fabrication tolerances, and manufacturers' proprietary issues. However, we can estimate a realistic *range* for component values based on the literature. Simulating the nose-to-nose calibration over this range allows us to estimate an expected range of errors due to the sampling circuitry. The methodology we develop can easily be applied to other sampling-circuit models or representations.

Numerical study yields information we would have difficulty obtaining through other methods. For example, unambiguous measurements of the response of the internal circuitry of high-speed samplers is extremely difficult to carry out. In addition, simulations enable parametric variation of circuitry that would be impossible to conduct experimentally due to limitations in the technology of component fabrication and measurement. Thus, parametric variation within numerical simulation offers insight into sampling-circuit-related error mechanisms in the nose-to-nose calibration that otherwise would not be available. More details about this work can be found in [4].

---

[1] SPICE is an acronym for "Simulation Program with Integrated Circuit Emphasis." The SPICE3 program that we use was developed by researchers at the University of California at Berkeley.

2. Background

The nose-to-nose calibration technique [5-8] was proposed in 1990 to determine the impulse response of broadband oscilloscopes. Finding and correcting the response of these high-speed oscilloscopes is important because the typical response time of their own internal sampling circuitry is of the same order as the signal-transition times of many high-speed circuits under test. While well-established methods exist for finding the amplitude response of broadband sampling oscilloscopes[2], the phase response has presented a more difficult challenge. The nose-to-nose calibration currently represents one practical method for estimating an oscilloscope's phase response.

One important application of nose-to-nose calibrated oscilloscopes is for phase calibration of certain types of nonlinear vector network analyzers (NVNAs). NVNAs allow measurement of the phase and amplitude response of nonlinear circuits and systems subjected to periodic stimuli. The nose-to-nose calibration enables phase correction of measured harmonic components relative to the fundamental. A transfer standard (typically a "reference" or "comb" generator that is rich in harmonic content) is first measured using a nose-to-nose-calibrated oscilloscope. The comb generator is then connected to the NVNA and the phase relationships of the comb generator's harmonics are measured on the NVNA. Since the phase relationships of the comb generator are known from the calibrated oscilloscope measurement, correction factors for the NVNA can be extracted and subsequent NVNA measurements corrected. Using this method, we can correct the phase relationship between the fundamental and harmonics of DUTs measured on NVNAs up to 50 GHz, although most NVNAs are currently limited to an upper frequency of 20 GHz.

The nose-to-nose calibration is a variation of a traditional method for correcting the phase response of broadband sampling oscilloscopes [9, 10]. In the traditional method, a well-characterized waveform is measured with the oscilloscope. The output of the oscilloscope is a convolution of this known signal with the impulse response of the oscilloscope. Once the impulse response of the oscilloscope is deconvolved from the measured signal, correction coefficients are extracted from the difference between the known and measured signals.

This traditional method has been difficult to implement for high-speed oscilloscopes since it is difficult to characterize a pulse where frequency content is on the order of the oscilloscope's input bandwidth (although recently electro-optic sampling has been proposed for this purpose [11, 12]). In the nose-to-nose calibration, the "known" pulse is the kickout pulse, which is generated when an offset voltage is applied to the bias

[2] To measure the amplitude response of broadband (defined here as 20 GHz or greater) oscilloscopes, we currently use the "swept-sine" method [9,13], where a series of individual tones of increasing frequency and known power are fed into the oscilloscope. The power in the tones is measured with a power meter traceable to a national standards laboratory. Comparing the known amplitude of the input signal to the signal measured by the oscilloscope allows us to determine and correct the magnitude response of the oscilloscope.

lines of the oscilloscope's sampling circuit. The kickout pulse is assumed to have essentially the same shape as the impulse response of the oscilloscope itself [5].

The nose-to-nose calibration requires very little custom equipment, and its sources of uncertainty have been studied in depth. Several researchers have investigated experimental sources of error in the nose-to-nose calibration [6-8, 13-15]. Others have analytically studied the errors introduced by the sampler circuitry of the oscilloscope itself [16, 17]. Here we turn to SPICE-based numerical simulation of a realistic model of the sampling circuit [1, 2] to better identify error mechanisms involving the internal sampling circuitry and to understand the sensitivity of the oscilloscope's phase response to parametric changes in values of sampling-circuit components. We develop procedures to quantify the sensitivity of the phase error to each component and to a combination of components, and then apply these procedures to our simulation results.

3. Sampling Circuitry and Error in the Nose-to-Nose Calibration

The error in the nose-to-nose calibration was defined in [1] and [3] as the difference between the nose-to-nose derived impulse response of a sampling circuit and the circuit's true impulse response. In our simulations, we derive the "true" impulse response using the procedure described in Refs. [9, 10] which deconvolves a known pulse from the output response of the sampler. We simulate the nose-to-nose measurement procedure by convolving the output of the sampler that is acting as a kickout generator with the impulse response of a second identical sampler. Because the nose-to-nose calibration assumes that the kickout pulse and impulse response have the same time-domain response, the kickout pulse is deconvolved from the output of the second sampler by taking the square root in the frequency domain.

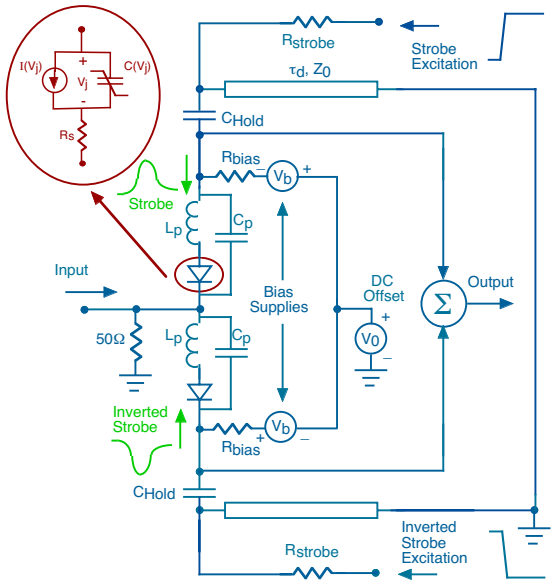

Figure 1: Schematic of the type of two-branch sampling circuit used in nose-to-nose measurements and in our SPICE simulations. The inset shows the large-signal equivalent circuit of the sample diode.

Table 1: Parameters of the default sampling-circuit model used in our simulations (see Fig. 1). Diode parameters are defined in the text. Other circuit parameters are: hold capacitor, C_H; reverse bias on the diodes, V_{bias}; strobe excitation pulse voltage, *Strobe*; rise time of the strobe excitation pulse, *Strobe rise*; and packaging parasitics that would be present in discrete diode packages, *Packaging*.

Diode Parameters						Circuit Parameters					
R_s (Ω)	I_s (pA)	n	C_{j0} (fF)	ϕ_{bi} (V)	γ	C_H (pF)	V_{bias} (V)	R_{bias} (Ω)	Strobe (V)	Strobe Rise (ps)	Packaging (pF/nH)
19	26.7	1.08	45	0.7	0.5	4.0	1.63	3600	12	10	--

Table 2: Summary of Default SPICE Simulation Settings

Simulation Parameter	Value
Maximum Time Step, t_{step}	0.5 ps
Sampling-Cycle Period, t_{samp}	500 ps
Input Voltage Level, v_{in}	0.2 V
Input Pulse Width, t_{pw}	0.5 ps

We developed a model [1, 2] of the sampling circuitry that is used in two-diode balanced oscilloscopes, based on a disassembled sampler head described in Ref. [18]. The model, its parameter values, and SPICE simulation settings are shown in Fig. 1, Table 1, and Table 2, respectively. We have modified the circuit of [18] to better reflect modern oscilloscopes. Specifically, we used a faster strobe excitation rise-time to better approximate oscilloscopes with 50 GHz input bandwidth, and we eliminated the packaging parasitics to better approximate modern monolithic diode structures.

The balanced configuration of the sampler means the strobe pulse (used to turn the diodes on and off during each sampling cycle) will cancel at both the input and output ports. The strobe source uses a step generator that drives a shorted transmission line connected in parallel with the sampling diode circuitry (see Fig. 1). A sharp voltage step initially turns the sampling diodes on. Reflection of the step from the shorted end of the transmission line turns the diodes off at $2\tau_d$, where τ_d is the transmission-line delay. We used a two-section ladder network to implement the transmission line in SPICE.

The sampling diode parameters listed in Table 1 are primarily defined by the large-signal equations for current and capacitance. The large-signal forward-bias current through a Schottky–barrier diode (see inset of Fig. 1) can be given by [19]

$$I(V_j) = I_s\left(\exp\left(\frac{qV_j}{nkT}\right) - 1\right), \tag{1}$$

where V_j is the large-signal voltage across the diode junction (not including the voltage drop, V_{RS}, across the spreading resistance R_s), I_s is the reverse saturation current, q is the

charge on an electron ($1.6\text{x}10^{-19}$ coulomb), n is the ideality factor, T is the junction temperature (K), and k is the Boltzmann constant ($1.38\text{x}10^{-23}$ J/K). The junction capacitance is given by

$$C_{\mathrm{j}}(V_{\mathrm{j}}) = \frac{C_{\mathrm{j0}}}{\left(1 - \dfrac{V_{\mathrm{j}}(t)}{\phi_{\mathrm{bi}}}\right)^{\gamma}}, \tag{2}$$

where C_{j0} is the zero-bias junction capacitance (Note $C_{\mathrm{j}} = C_{\mathrm{j0}}$, a constant, when $V_{\mathrm{j}} = 0$. This is an important concept in our nose-to-nose error calculations), ϕ_{bi} is the junction's built-in potential, and γ is the grading coefficient ($\gamma = 0.5$ for Schottky-barrier diodes and for linearly graded junctions in *pn*-type diodes [20]). The spreading resistance, R_{s}, models the loss behavior of the diode when it is strongly conducting. See the inset of Fig. 1 for the large-signal model of the diode.

Our simulations were performed in the time domain in SPICE and then transformed to the frequency domain by use of the fast-Fourier transform (FFT) procedure[3]. The sampler's impulse response was derived using the traditional method described in Section 2 and compared to the FFT of a nose-to-nose derived impulse response. This comparison generates the correction factor, $E(f)$, defined in [3] as the ratio of the estimate of the impulse response to the true impulse in the frequency domain:

$$E_{\mathrm{A}}(f) \equiv \frac{H_{\mathrm{A}}^{\mathrm{est}}(f)}{H_{\mathrm{A}}(f)} \cong C\sqrt{\frac{K_{\mathrm{B}}(f)}{H_{\mathrm{B}}(f)}}, \tag{3}$$

where $H(f)$ refers to the frequency-domain representation of the sampler's impulse response, $K(f)$ refers to the kickout pulse in the frequency domain, and the subscripts A and B refer to two different samplers. In our simulations, we used identical samplers, so the subscripts are not significant. The magnitude and phase components of the nose-to-nose derived impulse response were calculated respectively as

$$\left|E_{\mathrm{A}}(f)\right| = C\left|\sqrt{\frac{K_{\mathrm{B}}}{H_{\mathrm{B}}}}\right| \tag{4a}$$

$$\arg\left\{E_{\mathrm{A}}(f)\right\} = \frac{1}{2}\left[\arg\left\{K_{\mathrm{B}}(f)\right\} - \arg\left\{H_{\mathrm{B}}(f)\right\}\right], \tag{4b}$$

where we chose C in (4a) such that $E(0) = 1$, with $f = 0$ at the DC point. The linear part of the phase component (corresponding to an arbitrary time-shift introduced into a signal that passes through the sampler) was subtracted. Refer to Ref. [4] for more detail.

The magnitude and phase of $E(f)$ are plotted in Fig. 2 for the default SPICE model of the sampler. For the default sampling circuit configuration that we examined, our magnitude error is approximately 0.25 dB, which is lower than the approximately 0.6 dB

---

[3] We define the Fourier Transform as $F(\omega) = \int_{-\infty}^{\infty} f(t)e^{-j\omega t}dt$, with $\omega = 2\pi f$ and f the frequency, in Hertz.

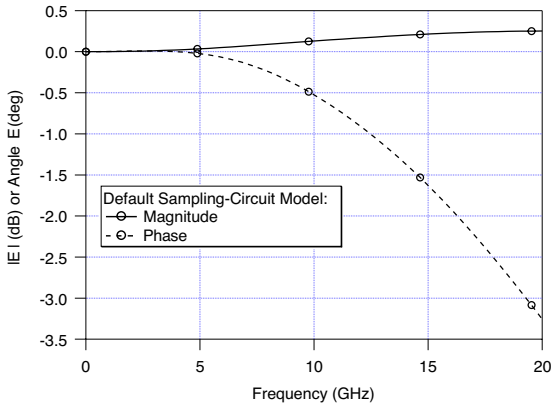

Figure 2: Magnitude and phase of $E(f)$ for the default sampling-circuit model. The curves show the difference between the impulse response of the sampler and the nose-to-nose derived impulse response estimate.

difference between a swept-sine and a nose-to-nose calibrated oscilloscope impulse response, as measured in [13]. Our phase error is approximately 3.3° at 20 GHz. This is on the order of the phase difference between an EOS measurement and a nose-to-nose calibrated oscilloscope measurement given in [11]. These differences between measured results and our sampling circuit are reasonable, since the measurements involved complete oscilloscopes and our model only approximates the sampling circuitry.

4. Parametric Studies

We investigated the sensitivity of the nose-to-nose calibration to variation in sampling-circuit component values by systematically varying individual circuit element values in our default sampling circuit model and noting changes in the magnitude and phase of the correction factor, $E(f)$. The results of these simulations clearly demonstrate which sampling circuit elements dominate the phase error in the nose-to-nose calibration and how sensitive the phase error is to variation in component values.

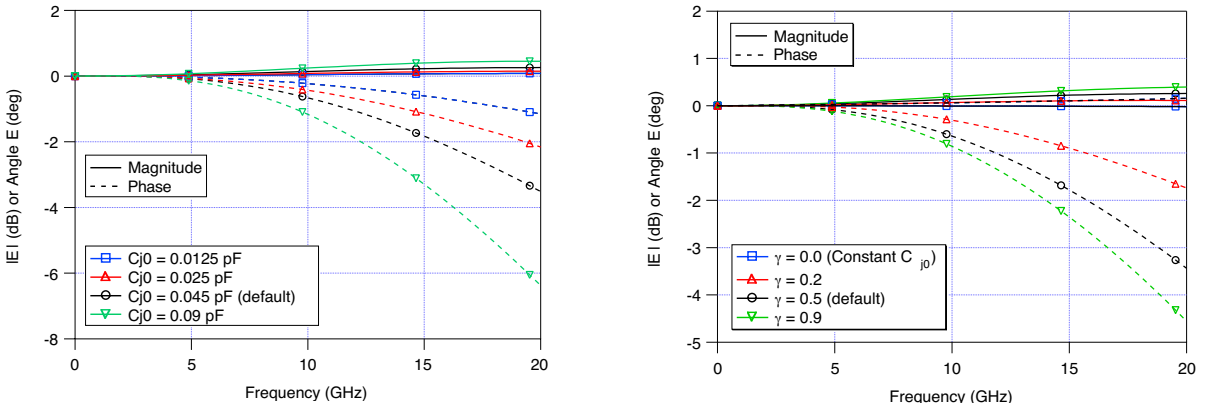

Figure 3: Magnitude and phase components of $E(f)$ for (a) different values of zero-voltage diode junction capacitance, C_{j0}; (b) various values of grading coefficient, γ. Note that the error in the nose-to-nose calibration is nearly zero when the junction capacitance is constant (for $\gamma = 0.0$, a physical impossibility). This suggests that the nonlinearity of the junction capacitance contributes to the phase error. C_{j0} and other model parameter values are those of the default diode model specified in Table 1.

We present a subset of our parametric study results [4] in Figs. 3 – 6. Figure 3 shows that the nonlinearity of the diode's junction capacitance – whether from an increased C_{j0} or a change in grading coefficient γ – has a profound effect on the phase error [see Eqn. (2)]. This effect has also been discussed in [3, 17]. In [4] we found that the variation of other diode parameters had negligible effect on the phase error and, hence, have not include those results here.

Figure 4 shows that some of the strobe-generator parameters also can have a significant effect on the phase error. The severity of the increase in the phase error caused by the diode's nonlinear junction capacitance is increased for longer charge time of the diode's junction capacitance before the diode conducts. This charge time is influenced by the strobe excitation-pulse rise-time, as shown in Fig. 4(a). Figure 4(b) shows that smaller strobe-generator impedances lead to increased phase error. This effect, which is somewhat counter-intuitive, is explained in detail in Ref. [4]. Figure 4(c) shows that the amplitude of the strobe pulse minimally affects the phase error, as long as the strobe is large enough to turn the diode on strongly.

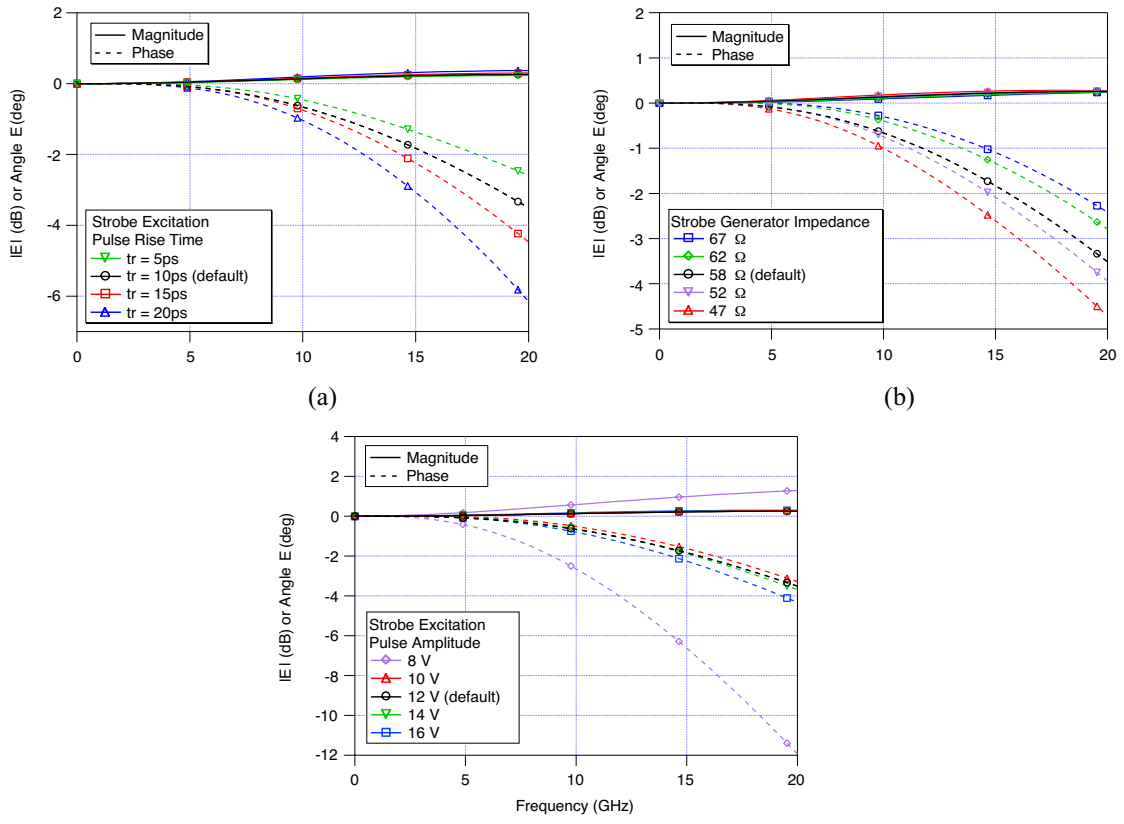

Figure 4: The effects of the strobe-generator model on the correction factor $E(f)$. (a) Strobe excitation-pulse rise times; (b) Strobe-generator impedance; (c) Strobe excitation-pulse amplitude. The 8 V strobe excitation pulse is not sufficient to turn the sampling diodes on properly and contributes strongly to error. The 8V case is neglected in the following section.

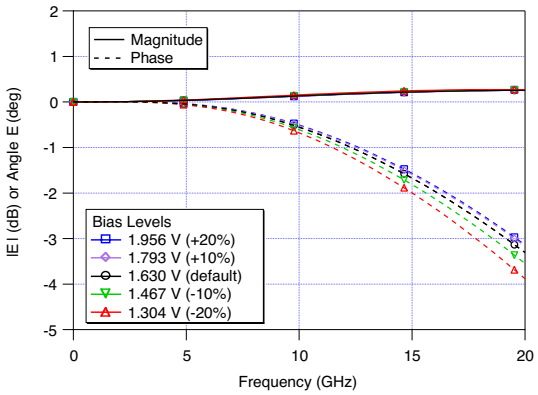

Figure 5: $E(f)$ for several bias levels up to +/-20% of the default model value.

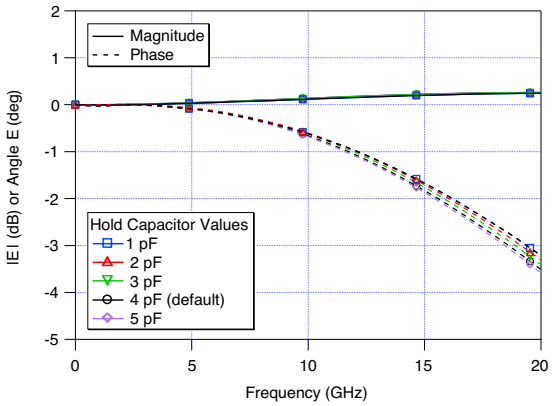

Figure 6: $E(f)$ as a function of the value of the hold capacitor.

We see in Figs. 5 and 6 that circuit parameters such as bias level and hold capacitor value have a less pronounced effect. The results of our parametric studies are quantified in the following section. More detail and an extensive discussion of these results can be found in Ref. [4].

5. Sensitivity Analysis

As we saw in Section 4, it is straightforward to find the total phase error for a particular sampler configuration. However, finding the "absolute" contribution of each parameter to the phase error for any arbitrary configuration is not possible since the effects of many parameters are correlated. An example of this was given in Section 4, where we discussed interaction of the junction capacitance and the strobe generator's excitation-pulse rise-time. Thus it is necessary to examine the sensitivity of the phase error of a given sampling-circuit model to changes in component value, rather than to find the specific contribution of a parameter to the total phase error.

In this section we develop procedures to quantify the sensitivity of the phase error in the nose-to-nose calibration to component-value variation. We develop two procedures and apply them to the parametric simulations we carried out for our representative sampling-circuit model. These procedures are not specific to our model and could easily be utilized in the characterization of other sampling-circuit models.

We first rank the circuit parameters listed in Table 1 with respect to impact on the phase error of the default sampling circuit for a given proportional change in component value (10 %). From this ranking, we see the relative effect that variation (or uncertainty) in the value of each circuit parameter has on the phase error of the calibration. This information can be used in a variety of ways, for example, in determining which circuit elements should be modeled most carefully in sampling-circuit simulations, and which circuit elements should be considered in sampling-circuit design for improved nose-to-nose calibrations.

The second procedure for examining the sensitivity of the phase error involves calculation of the standard uncertainty in the phase error due to *combined* variation in component values. This represents our best estimate of a *range* of phase error values inherent in the sampling circuitry for a real nose-to-nose calibration. Uncertainty exists in both the values of the circuit parameters and in the way some circuit elements are modeled. By assuming a significant level of uncertainty for each individual circuit parameter, we hope to cover the expected range of phase errors due to the sampling circuitry in a real nose-to-nose calibration.

In order to rank component effect on phase error (the first procedure above), we express the uncertainty in the phase error corresponding to each parameter in our default sampling circuit model as [21, 22]

$$u_{\phi}(\alpha_j) = \frac{\partial \phi}{\partial \alpha_j} u_{\alpha_j}, \tag{5}$$

where α_j = the circuit parameter value corresponding to parameter number j,
u_{α_j} = the fractional uncertainty (variation) in α_j (10 % of the values given in Table 1),
ϕ = the phase error in the nose-to-nose calibration simulations (with a default value of ~3.3°), and
$\frac{\partial \phi}{\partial \alpha_j}$ = the change in the phase error due to variation in the circuit parameter value α_j.

To compare the uncertainties expressed in (5), we performed simulations of our default model where we choose a fractional uncertainty u_{α_j} of +/-10 % (that is, $0.1\alpha_j$) for each model component value α_j listed in Table 1. We chose the same value for all fractional uncertainties to explore the relative sensitivity of the phase error to component value variation. In practice, each u_{α_j} depends on the characteristics of the individual sampling circuit. We selected a value of 10 % since this is the maximum variation in junction capacitance (based on manufacturer's data sheets) for sampling diodes that are similar to those we expect to find in the type of oscilloscopes used in nose-to-nose calibrations [23].

For each parameter, we calculated a minimum of three sets of phase errors: the default case, one (or more) case(s) with α_j increased, and one (or more) case(s) with α_j decreased. We fitted a straight line to these phase errors at 20 GHz (the highest frequency considered in our simulations) and numerically calculated the derivative $[\partial\phi/\partial\alpha_j]$ of this line. We fitted the change in phase error with a straight line since our typical change in error is expected to be small.[4] We then multiplied the derivative (a constant value) by the fractional uncertainty u_{α_j} to find the uncertainty in the phase error $u_{\phi}(\alpha_j)$ due to this particular parameter.

[4] For some parameters, this small-value approximation does not hold and some additional error is introduced into the uncertainty calculation.

Table 3: Uncertainty in the phase error in the nose-to-nose calibration at 20 GHz for the sampling-circuit parameter values listed in Table 1. Contributions are ranked from highest to lowest.

Parameter α_j	value of α_j	$u_{\alpha_j} = 0.1\alpha_j$	$\frac{\partial \phi}{\partial \alpha_j}$	$u_\phi(\alpha_j)$
Strobe Generator Impedance	28.5 Ω / branch	2.9 Ω	0.12°/Ω	0.35°
C_{j0}	0.045 pF	0.0045 pF	-70.0°/pF	0.32°
γ	0.5	0.05	-5.20°/unit	0.26°
Strobe Excitation Pulse Rise Time	10 ps	1 ps	-0.23°/ps	0.23°
Strobe Amplitude	12 V	1.2 V	-0.16°/V	0.20°
Bias Value	1.63 V	0.163 V	+1.15°/V	0.19°
N	1.08	0.108	-1.67°/unit	0.18°
C_H	4 pF	0.4 pF	-0.36°/pF	0.14°
ϕ_{bi}	0.7 V	0.07 V	+0.82°/V	0.06°
Embedding Impedance	50 Ω	5 Ω	-0.011°/Ω	0.05°
I_{sat}	20 pA	2 pA	+2.97e9°/A	0.01°
R_s	10 Ω	---	---	not significant source of error

Table 3 indicates that the strobe generator impedance has the most significant effect on the phase error for a fractional uncertainty of 10 % in α_j, followed closely by nonlinear diode junction capacitance. The effects of the strobe generator impedance and the diode junction capacitance on the error are shown in Figs. 4(b) and 3(a), respectively.

To estimate a range of phase errors for the nose-to-nose calibration (the second procedure described above), we first estimated an upper and lower bound on the phase error in the default sampler model. We performed simulations that incorporate combined parametric variation: We varied all of the circuit parameters simultaneously in such a way as to increase the phase error, and then varied all of the circuit parameters to decrease the phase error. As shown in Table 3, increasing some parameters increased the phase error ($[\partial\phi/\partial\alpha_j] > 0$), while increasing other parameters decreased the phase error ($[\partial\phi/\partial\alpha_j] < 0$).

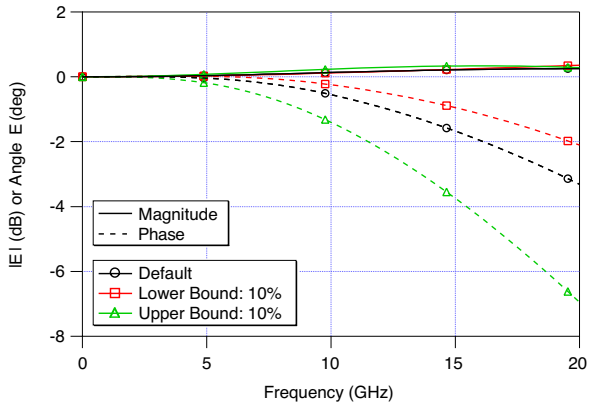

Figure 7: SPICE simulations of upper and lower phase error bounds with all parameters changed by 10 %.

Figure 7 shows the results of our combined parametric simulations with the value of all circuit parameters α_j changed simultaneously by 10 % in such a way as to increase or decrease the phase error. Note the typical default sampler phase error value of 3.32° at 20 GHz. We see an increase of 3.64° (to 6.96°) for the upper bound, and a decrease of 1.21° (to 2.11°) for the lower bound. Note that the change in the phase error is not symmetric about the default value. Refs. [21] and [22] address such a case and suggest using a standard uncertainty of

$$u_\phi = \frac{a}{\sqrt{3}}, \tag{6}$$

where $2a$ is the difference between the lower bound and the upper bound, and a is

$$a = \frac{b_- + b_+}{2}, \tag{7}$$

with b_+ the positive offset, and b_- the negative offset. Note that (6) corresponds to the standard deviation of a rectangular distribution from the lower bound to the upper bound, and (7) effectively shifts the mean to the middle of this distribution. The standard uncertainty is then given by

$$\begin{aligned} u_\phi(\alpha) &= \sqrt{\frac{(b_+ + b_-)^2}{12}} \\ &= \sqrt{\frac{(3.64^\circ + 1.21^\circ)^2}{12}}, \\ &= 1.4^\circ \end{aligned} \tag{8}$$

where α represents the combined set of circuit parameters. Our estimate of the phase error for our default sampling circuit model is then 3.32° +/-1.4° at 20 GHz, where 1.4° is the numerical value of standard uncertainty $u_\phi(\alpha)$ and not a confidence interval.

If we were to assume no correlation between the circuit parameters, the uncertainties $u_\phi(\alpha_j)$ listed in Table 3 would add in a root-sum-of-squares (RSS) sense to give the combined uncertainty, $u_\phi(\alpha)$, of 0.98°. If we were to assume complete correlation, the uncertainties listed in Table 3 would add directly, giving $u_\phi(\alpha)$ of 2.96°. We expect that the combined uncertainty for the phase error in the sampling circuit lies somewhere between these two, and our results support this contention.

6. Summary

We performed a sensitivity study of the effect of the variation of sampling-circuit parameters on the phase error in the nose-to-nose calibration using a SPICE model of the sampling circuit. We first defined a way to express the difference between our nose-to-nose-derived estimate of the impulse response of a sampler and the actual impulse response. We then observed the change in this error as we individually varied each circuit parameter. We ranked the circuit parameters in terms of most significant impact on the phase error for a given parametric variation (10 % of the default value), and found the standard uncertainty of the phase error with respect to this parametric variation.

We varied the combined component values in our default sampling circuit model, and calculated a phase error of 3.32° +/1.4°, where 1.4° is the numerical value of standard uncertainty. By assuming a significant level of uncertainty for each individual circuit parameter, our intent was to cover the expected range of phase errors in a real nose-to-nose calibration. This provides us with a first-cut estimate of the contribution of the sampling circuitry to the phase error in the nose-to-nose calibration, since, as mentioned in the Introduction, this quantity cannot be measured directly.

Our parametric studies indicate that both the diode's nonlinear junction capacitance and the strobe generator's impedance significantly influence the total phase error. Thus, we expect that refining the diode and strobe generator models will help to more accurately determine the inherent phase error in the nose-to-nose calibration due to the sampling circuitry.

Acknowledgement:

The author is grateful to the following people for help with models, theory, and discussion of the nose-to-nose calibration: Dylan Williams, Don DeGroot, Jan Verspecht, Marc Vanden Bossche, John Kerley, Paul Hale, Tracy Clement, Jim Randa.

References:

[1] D. F. Williams, K. A. Remley, and D. C. DeGroot, "Nose-to-nose response of a 20-GHz sampling circuit," *54th ARFTG Conf. Dig.*, pp. 64-70, Dec. 1999.

[2] K. A. Remley, D. F. Williams, and D. C. DeGroot, "Realistic Sampling-Circuit Model for a Nose-to-Nose Calibration," *IEEE MTT-S Int. Microwave Symp. Dig.*, pp. 1473-1476, June 2000.

[3] K. A. Remley, D. F. Williams, D. C. DeGroot, J. Verspecht, and J. Kerley, "Effects of nonlinear diode junction capacitance on the nose-to-nose calibration," *IEEE Microwave and Wireless Comp. Lett.*, vol. 11, pp. 196-198, May 2001.
[4] K. A. Remley, "The impact of internal sampling circuitry on the phase error inherent in the nose-to-nose oscilloscope calibration," *Natl. Inst. Stand. Technol. Tech. Note #1528*, 2002, submitted for publication.
[5] K. Rush, S. Draving, and J. Kerley, "Characterizing high-speed oscilloscopes," *IEEE Spectrum*, pp. 38-39, Sept. 1990.
[6] J. Verspecht and K. Rush, "Individual characterization of broadband sampling oscilloscopes with a nose-to-nose calibration procedure," *IEEE Trans. Instrum. Meas.*, vol. 43, pp. 347-354, Apr. 1994.
[7] J. Verspecht, "Broadband sampling oscilloscope characterization with the `nose-to-nose' calibration procedure: a theoretical and practical analysis," *IEEE Trans. Instrum. Meas.*, vol. 44, pp. 991-997, Dec. 1995.
[8] J. Verspecht, "Calibration of a Measurement System for High Frequency Nonlinear Devices." Brussels, Belgium: Vrije Univeriteit Brussels, Ph.D. Thesis, Sept. 1995.
[9] W. L. Gans, "Dynamic calibration of waveform recorders and oscilloscopes using pulse standards," *IEEE Trans. Instrum. and Measurement*, vol. 39, pp. 952-957, Dec. 1990.
[10] J. P. Deyst, N. G. Paulter, T. Daboczi, G. N. Stenbakken, and T. M. Souders, "A fast-pulse oscilloscope calibration system," *IEEE Trans. Instrum. and Measurement*, vol. 47, pp. 1037-1041, Oct. 1998.
[11] D. F. Williams, P. D. Hale, T. S. Clement, and J. M. Morgan, "Calibrating electro-optic sampling systems," *IEEE MTT-S Int. Microwave Symp. Dig.*, pp. 1527-1530, May 2001.
[12] D. Henderson, A. G. Roddie, and A. J. A. Smith, "Recent developments in the calibration of fast sampling oscilloscopes," *IEE Proc. A*, vol. 139, pp. 254-260, Sept. 1992.
[13] P. D. Hale, T. S. Clement, K. J. Coakley, C. M. Wang, D. C. DeGroot, and A. P. Verdoni, "Estimating the magnitude and phase response of a 50 GHz sampling oscilloscope using the `Nose-to-Nose' method," *55th ARFTG Conf. Dig.*, pp. 35-42, June 2000.
[14] D. C. DeGroot, P. D. Hale, M. Vanden Bossche, F. Verbeyst, and J. Verspecht, "Analysis of interconnection networks and mismatch in the nose-to-nose calibration," *55th ARFTG Conf. Dig.*, pp. 116-121, June 2000.
[15] D. R. Larson and N. G. Paulter, "The effects of offset voltage on the amplitude and bandwidth of kick-out pulses used in the nose-to-nose sampler impulse response characterization method," *IEEE Trans. Instrum. Meas.*, vol. 50, pp. 872-876, Aug. 2001.
[16] J. Verspecht, "Quantifying the maximum phase-distortion error introduced by signal samplers," *IEEE Trans. Instrum. Meas.*, vol. 46, pp. 660-666, June 1997.
[17] D. F. Williams and K. A. Remley, "Analytic sampling-circuit model," *IEEE Trans. Microwave Theory Tech.*, vol. 49, pp. 1013-1019, June 2001.
[18] S. Riad, "Modeling of the HP-1430A feedthrough wideband (28-ps) sampling head," *IEEE Trans. Instrum. Meas.*, vol. IM-31, pp. 110-115, June 1982.
[19] S. A. Maas, *Microwave Mixers*, 2nd ed. Boston, MA: Artech House, 1993.
[20] G. W. Neudeck, *The PN Junction Diode, 2nd ed.* Reading, MA: Addison-Wesley, 1989.
[21] American National Standards Institute, "U. S. Guide to the Expression of Uncertainty in Measurement." Boulder, CO: National Conference of Standards Laboratories, 1997.
[22] International Organization for Standardization (ISO), "Guide to the Expression of Uncertainty in Measurement." Geneva, Switzerland, 1995.
[23] Agilent Technologies Inc., "Data Sheet: HSCH-9101/9201/9251 GaAs Beam Lead Schottky Barrier Diodes," 2001.